


Estimate of the Upper Limit on Hot Plasma Differential Emission Measure (DEM) in Non-Flaring Active Regions and Nanoflare Frequency Based on the Mg XII Spectroheliograph Data from CORONAS-F/SPIRIT

Anton Reva¹  · Artem Ulyanov¹ · Alexey Kirichenko¹ · Sergey Bogachev¹ · Sergey Kuzin¹

© Springer ●●●

Abstract The nanoflare-heating theory predicts steady hot plasma emission in the non-flaring active regions. It is hard to find this emission with conventional non-monochromatic imagers (such as *Atmospheric Imaging Assembly* or *X-Ray Telescope*), because their images contain a cool temperature background. In this work, we search for hot plasma in non-flaring active regions using the Mg XII spectroheliograph onboard *Complex Orbital Observations Near-Earth of Activity on the Sun (CORONAS)-F/Spectroheliograph* *X-ray Imaging Telescope (SPIRIT)*. This instrument acquired monochromatic images of the solar corona in the Mg XII 8.42 Å line, which emits only at temperatures higher than 4 MK. The Mg XII images contain the signal only from hot plasma without any low-temperature background. We studied the hot plasma in active regions using the SPIRIT data from 18–28 February 2002. During this period, the Mg XII spectroheliograph worked with a 105-second cadence almost without data gaps. The hot plasma was observed only in the flaring active regions. We do not observe any hot plasma in non-flaring active regions. The hot plasma column emission measure in the non-flaring active region should not exceed $3 \times 10^{24} \text{ cm}^{-5}$. The hot Differential Emission Measure (DEM) is less than 0.01% of the DEM of the main temperature component. Absence of Mg XII emission in the non-flaring active regions can be explained by weak and frequent nanoflares (delay less than 500 seconds) or by very short and intense nanoflares that lead to non-equilibrium ionization.

Keywords: Flares, Microflares and Nanoflares; Heating, Coronal

✉ A. A. Reva
reva.antoine@gmail.com

¹ Lebedev Physical Institute of Russian Academy of Sciences, Leninskij Prospekt 53, Moscow 119991, Russia

1. Introduction

The solar corona has a temperature around 1 MK, which is much higher than the temperature of the photosphere. It is unknown why the corona is so hot.

Today, there are two main theories of the coronal heating: by nanoflares and by MHD waves. Nanoflare theory assumes that many small-scale flares (nanoflares) occur in the corona (Parker, 1988; Klimchuk, 2015). The nanoflares result from small-scale reconnection episodes. Although the energy of each nanoflare is small, their total energy could be sufficient to heat the corona.

In the wave theory, the photosphere generates MHD waves that propagate to the corona, where they dissipate and heat the corona (Biermann, 1948; Davila, 1987; Schwarzschild, 1948). Waves can produce high-frequency small-scale events that will be indistinguishable from nanoflares (Klimchuk, 2006). For this reason, we will use the term “nanoflare” to denote a small-scale impulsive energy release event without regard to its nature (waves or reconnection).

Both nanoflares and waves (that propagate from the photosphere to the corona) are hard to detect directly. That is why the experimental tests of these models are focused on finding “observables” that these models predict.

One such observable is faint emission of hot plasma (temperature greater than 4 MK) in non-flaring active regions. If the delay between nanoflares on an individual field line is less than the loop cooling time (high-frequency heating), the loop is heated by weak and frequent nanoflares and its temperature slightly deviates from the average value. If the delay between nanoflares is greater than the loop cooling time (low-frequency heating), the loop is heated by stronger but less-frequent nanoflares. In this case, the loop temperature will significantly deviate from the average value. To maintain the average coronal temperature, the nanoflare should heat the loop to temperatures greater than 4 MK. Due to the large number of nanoflares, this will create a steady hot-plasma faint emission (Cargill, 1994, 2014; Klimchuk, 2015). Detection of hot plasma in non-flaring active regions would be an indirect evidence of low-frequency nanoflare heating. Absence of hot emission can help to constrain the nanoflare frequency.

However, it is hard to find faint hot-plasma emission with conventional non-monochromatic imagers—like the *Atmospheric Imaging Assembly* (AIA: Lemen *et al.*, 2012) or the *X-Ray Telescope* (XRT: Golub *et al.*, 2007)—because their images contain a cool temperature background. Although some researchers (Reale *et al.*, 2011; Warren, Winebarger, and Brooks, 2012; Testa and Reale, 2012) have developed methods to subtract most of the cold background from AIA images, the resulting data still contain the mixed signal, which comes from the hot and cold plasma.

Reale *et al.* (2009), Schmelz *et al.* (2009a,b), and Testa *et al.* (2011) reported detection of hot plasma using XRT data. However, Winebarger *et al.* (2012) showed that the XRT data cannot be used to confirm the existence of hot plasma with low emission measure. Due to the broad temperature-response function of the XRT, the instrument can only detect hot plasma with an emission measure that is higher than 10% of the emission measure of the warm component (≈ 2 –3 MK).

Several researchers have studied hot plasma in non-flaring active regions using monochromatic observations. In hard X-ray, the observations were made with focusing hard X-ray telescopes: *Nuclear Spectroscopic Telescope Array* (NuSTAR: Hannah *et al.*, 2016; Harrison *et al.*, 2013) and *Focusing Optics X-ray Solar Imager* (FOXSI: Ishikawa *et al.*, 2014; Krucker *et al.*, 2014). In soft X-ray, non-imaging spectrometers were used: *Solar Maximum Mission (SMM)/Flat Crystal Spectrometer (FCS)* (Del Zanna and Mason, 2014), *Solar PHotometer IN X-rays* (SphinX: Miceli *et al.*, 2012; Gburek *et al.*, 2011), and *REntgenovskiy Spectrometer s Izognutymi Kristalami* (RESIK: Sylwester, Sylwester, and Phillips, 2010; Sylwester *et al.*, 2005). In the EUV range, the observations were made with imaging spectrometers: *Solar Ultraviolet Measurement of Emitted Radiation* (SUMER: Parenti *et al.*, 2017; Wilhelm *et al.*, 1995) and *Extreme Ultraviolet Normal Incidence Spectrograph* (EUNIS-13: Brosius, Daw, and Rabin, 2014). These works estimated upper limit on the emission measure of the hot plasma in non-flaring active regions.

To test the nanoflare-heating model, we need some way to measure the quantity of the hot plasma (≈ 10 MK) relative to warm plasma (temperature at DEM maximum, ≈ 3 MK). At the same time, we need enough images of hot plasma to distinguish non-flaring active regions from flaring ones.

For this purpose, we need at least two imaging instruments. The first one should be sensitive to hot plasma and at the same time blind to cool plasma. The second one should image the cool plasma. The instruments should be cross-calibrated and have a rapid enough cadence to observe the dynamics of the hot plasma.

In this paper, we try to set an upper limit on the hot-plasma differential emission measure (DEM) using direct observations of the hot plasma by the Mg XII spectroheliograph (Zhitnik *et al.*, 2003) onboard *Complex Orbital Observations Near-Earth of Activity on the Sun (CORONAS)-F/Spectroheliograph Ic X-ray Imaging Telescope (SPIRIT)* (Oraevsky and Sobelman, 2002; Zhitnik *et al.*, 2002). This instrument imaged coronal hot plasma without low-temperature background. We will compare the obtained limit with the result of recent numerical simulations and will try to put constraints on the parameters of the nanoflare-heating model.

2. Experimental Data

In our research, we use the data of the Mg XII spectroheliograph and the data of the *Extreme ultraviolet Imaging Telescope* (EIT: Delaboudinière *et al.*, 1995).

The Mg XII spectroheliograph (Zhitnik *et al.*, 2003) onboard CORONAS-F/SPIRIT (Oraevsky and Sobelman, 2002; Zhitnik *et al.*, 2002) obtained monochromatic images of the solar corona in the Mg XII 8.42 Å line. This line emits only at temperatures higher than 4 MK. The Mg XII images differ from images of other “hot imagers” (like AIA or XRT); they do not contain a solar limb or any other low-temperature background. For a comparison of the Mg XII images with other “hot imagers”, see Reva *et al.* (2012, 2015). Temperature-response function of the Mg XII spectroheliograph is shown in Figure 1.

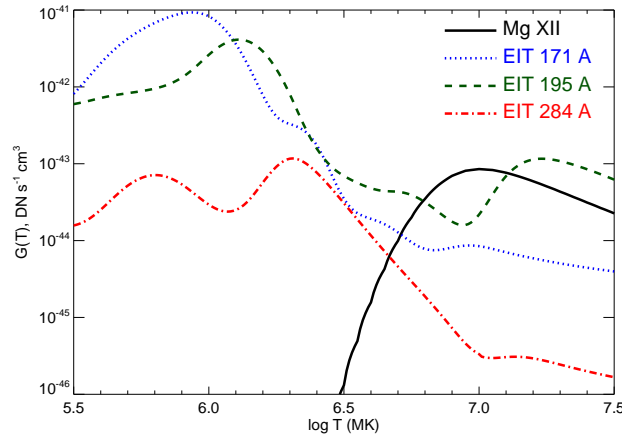


Figure 1. Temperature response functions of the Mg XII spectroheliograph and EIT channels. Black solid curve: the Mg XII spectroheliograph; blue dotted curve: EIT 171 Å; green dashed curve: EIT 195 Å; red dash dotted curve: EIT 284 Å.

We studied the period from 18–28 February 2002. At this time, the Mg XII spectroheliograph worked with a 105-second cadence almost without data gaps. In these observations, the Mg XII spectroheliograph registered binned images with a spatial resolution of $8''$ and a 37 s exposure time.

The Mg XII data were preprocessed: we subtracted the bias and dark-current frames. After preprocessing, the accuracy of the zero (average pixel count in the areas without hot objects) was ≈ 0.5 DNs, and the value of the noise was ≈ 6 DNs. The main source of the noise was an electronic interference. In binned Mg XII images, a single photon causes ≈ 7 DNs.

The EIT telescope onboard the *Solar and Heliospheric Observatory (SOHO)* spacecraft (Domingo, Fleck, and Poland, 1995) took solar images at the wavelengths centered at 171, 195, 285, and 304 Å. In a synoptic mode, EIT took images in all four channels every six hours; in the “CME watch” mode, the telescope took images in the 195 Å channel every 12 minutes. The pixel size of the telescope is $2.6''$, and the spatial resolution is $5''$. The temperature response functions of the EIT 171, 195, and 284 channels are shown in Figure 1. EIT data were preprocessed with the standard `eit_prep.pro` procedure from the Solar Software package.

3. Results

3.1. Hot Plasma on the Sun

The Electronic Supplementary Material movie of Figure 2 shows the hot-plasma dynamics observed by the Mg XII spectroheliograph. Only two types of hot objects were present on the Sun: the first is small isolated flare-like phenomena (Reva *et al.*, 2012). During the period of observations, they occur at a rate of

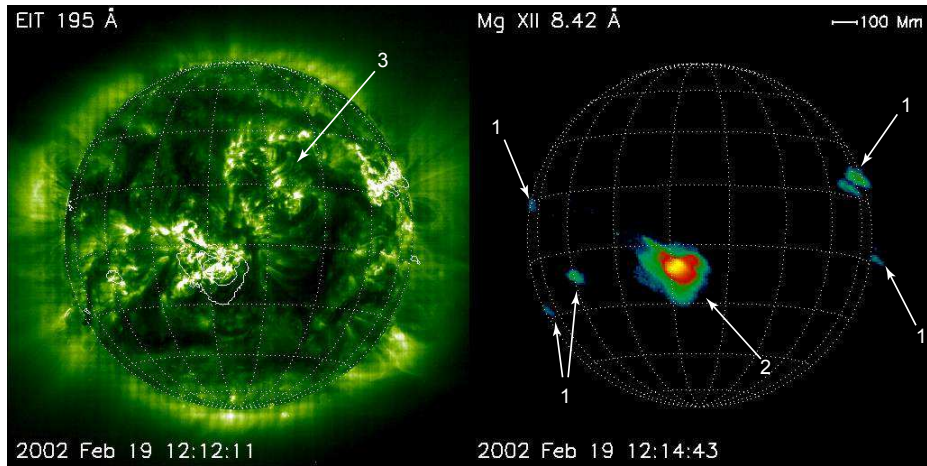


Figure 2. Hot plasma observed by the Mg XII spectroheliograph. Left: the EIT image; right: the Mg XII spectroheliograph image (*blue and green* correspond to low intensities, *red and yellow* to high intensities). 1) small flare-like objects; 2) flaring active region with hot plasma; 3) non-flaring active region without hot plasma. (An Electronic Supplementary Material of this figure is available.)

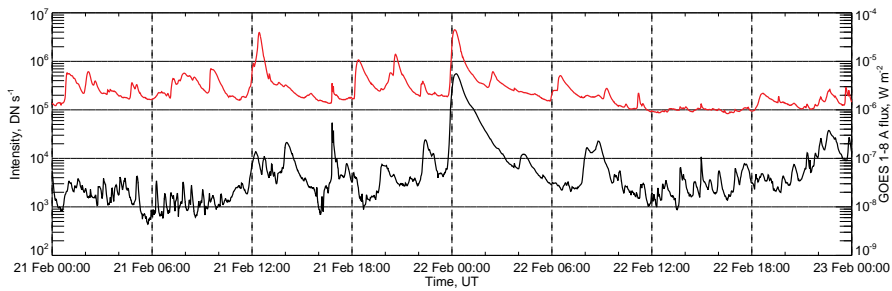


Figure 3. Black: the Mg XII spectroheliograph lightcurve of the flaring active region NOAA 09830; red: GOES 1–8 Å flux. This active region is marked with “2” in Figure 2.

20 per day. The second is large hot structures inside active regions. These are produced during flares or sequences of microflares. Their X-ray emission is highly variable (see Figure 3). After the flare ends, these large structures fade away.

Except for rare microflares, there was no hot plasma in non-flaring active regions. Below we discuss this fact and try to estimate the upper limit of the hot-plasma emission measure and nanoflare frequency, which may be consistent with this lack of signal.

3.2. Upper Limit on Hot Plasma in Non-Flaring Active Regions

Although we do not observe hot plasma in non-flaring active regions, it is possible that its emission is so faint that the Mg XII spectroheliograph cannot detect it. Nonetheless, we can estimate the upper limit on the amount of hot plasma using the sensitivity threshold of the instrument.

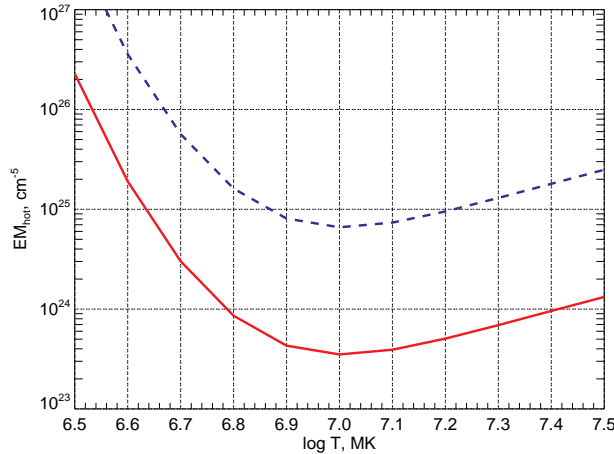


Figure 4. Upper limit on the column emission measure of hot plasma in non-flaring active regions. Red solid curve: upper limit derived from the noise of the Mg XII spectroheliograph; blue dashed curve: upper limit derived from the average pixel count.

For the estimate, we assume that the prediction of the nanoflare-heating model is correct: every pixel of the non-flaring active region has a small amount of hot plasma. We do not observe it, because its emission in the Mg XII line [I_{hot}] is lower than the minimal signal that the Mg XII spectroheliograph can detect [I_{min}].

I_{hot} is expressed as

$$I_{\text{hot}} = EM_{\text{hot}}G(T), \quad (1)$$

where EM_{hot} is the column emission measure of the hot plasma, and $G(T)$ is the temperature response function of the Mg XII spectroheliograph.

Hence, the upper limit on the column emission measure of hot plasma in non-flaring active regions is

$$EM_{\text{hot}} = \frac{I_{\text{hot}}}{G(T)} \leq \frac{I_{\text{min}}}{G(T)}. \quad (2)$$

Two factors determine I_{min} . The first one is the noise of the instrument: we cannot detect the signal that is lower than the noise. The second one is the photon statistics: we cannot detect less than one photon. I_{min} is the largest of the instrument noise and counts caused by a single photon.

Mg XII images with a 37-second exposure had a noise of $N \approx 6$ DNs. In binned Mg XII images, a single photon caused $I_{\text{phot}} \approx 7$ DNs. Since $I_{\text{phot}} > N$, then $I_{\text{min}} = I_{\text{phot}}$. We put the value of I_{phot} into Equation 2 and calculated the upper limit on the EM_{hot} (see Figure 4, blue). The column emission measure of hot plasma ($T \geq 5$ MK) should not exceed $5 \times 10^{25} \text{ cm}^{-5}$.

We made this estimate based on the absence of the signal in a single CCD pixel. However, each pixel of the non-flaring active region should contain hot plasma. If we integrate the signal in all pixels of the active region, the photon

statistics will improve and the influence of the noise will decrease. This procedure could make our estimate better constrained.

For the analysis, we chose the active region NOAA 09833 (see Figure 5). Except for a few microflares, there were no flares in this active region. The size of the area is 83×90 pixels. We averaged the flux of the chosen active region in the Mg XII line. The average pixel count amounted to -0.4 DN.

During averaging, the noise should decrease by a factor of \sqrt{K} ($K = 83 \times 90$ is the number of pixels) and amount to ≈ 0.05 DN. The minimal average detectable signal caused by photon statistics should be one photon divided by the number of pixel (≈ 0.001 DN). The absolute value of the average pixel count coincides with the error of the preprocessing.

As we see, after averaging, the noise and the photon statistics do not limit the sensitivity. The accuracy of the preprocessing determine the sensitivity threshold. We will use it as an upper limit on the signal from the hot plasma.

We put the absolute value of the average pixel count into Equation 2 and calculated the upper limit on the column emission measure (see Figure 4, red). The column emission measure of hot plasma ($T \geq 5$ MK) should not exceed $3 \times 10^{24} \text{ cm}^{-5}$.

3.3. DEM of the Active Region

To estimate the relative amount of the hot and warm (main temperature component) plasma, we reconstructed the DEM of the non-flaring active region NOAA 09833 (see Figure 5). For the selected active region, we extracted its fluxes from the Mg XII, EIT 171, 195, and 284 Å channels. During extraction, we summed the signal inside the rectangle marked in the Figure 5. For the EIT channels, we subtracted from the fluxes the average flux of the quiet Sun multiplied by the area of the rectangle. The flux of the quiet Sun was calculated as the mean intensity on the boundary of the rectangle.

Using these four fluxes, we reconstructed the DEM with a genetic algorithm. To find a solution that fits the experimental fluxes, the method minimizes χ^2 by mimicking the process of natural selection. The algorithm is described in Appendix A.

Due to its random nature, the genetic algorithm returns different DEMs on different runs. Each of these solution satisfy the experimental fluxes equally well. If we run the algorithm multiple times, the spread of the solutions will be an estimate of the reconstruction accuracy. The accuracy is determined not by the method or measurement errors, but by the data set.

We ran the algorithm 100 times and plotted the result in the Figure 6. The amount of plasma with $T = 5$ MK ($\log T = 6.7$) is four orders of magnitude lower than the main temperature component, and the amount of plasma with $T = 10$ MK is four to five orders lower.

At $\log T \geq 7.0$, only the Mg XII flux constrains the DEM. The DEM in Figure 6 at $\log T \geq 7.0$ shows the values that could be added to the DEM without increasing the Mg XII flux to a level greater than the noise. These values are the DEM upper limit.

The Mg XII spectroheliograph and EIT are not cross calibrated. The uncertainties in the cross calibration could affect the DEM reconstruction: the

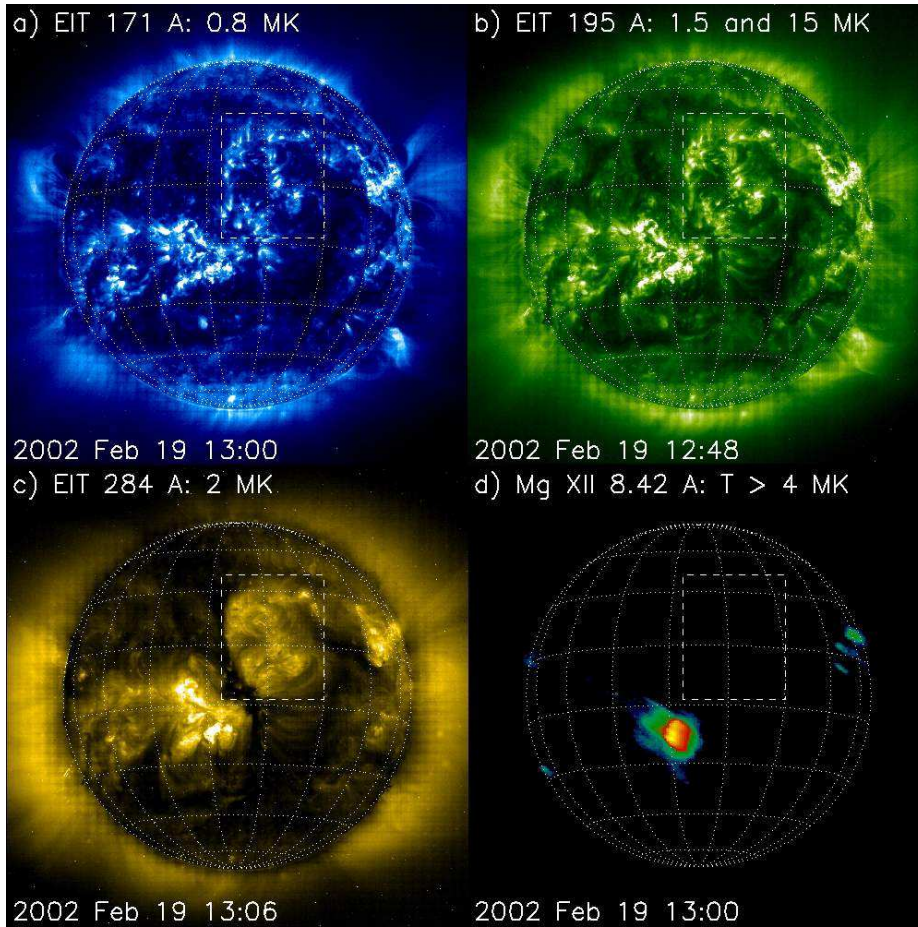


Figure 5. Non-flaring active region NOAA 09833 that was used to determine DEM. a) EIT 171 Å image; b) EIT 195 Å image; c) EIT 284 Å image; d) spectroheliograph Mg XII image. Rectangle marks the active region that was used for DEM measurements.

purple curve on Figure 6 could move up or down. Below we will estimate the uncertainties in the cross calibration.

During large flares the Mg XII flux is proportional to the GOES flux (Urnov *et al.*, 2007). Using this fact, the Mg XII spectroheliograph was cross calibrated with GOES. The accuracy of the correlation between GOES and Mg XII is $\approx 10\%$ (Urnov *et al.*, 2007). The accuracy of the GOES calibration is $\approx 30\%$ (White, Thomas, and Schwartz, 2005; Viereck and Machol, 2017). During cross calibration the CHIANTI atomic database (Dere *et al.*, 1997) was used, which has an accuracy of $\approx 20\%$ (Del Zanna, O’Dwyer, and Mason, 2011). This gives us a total accuracy of the Mg XII spectroheliograph calibration of $\approx 60\%$.

Depending on the channel, the precision of the EIT calibration varies from 60 to 150% (Dere *et al.*, 2000). For the sake of the estimate, we will use the mean value of 100%.

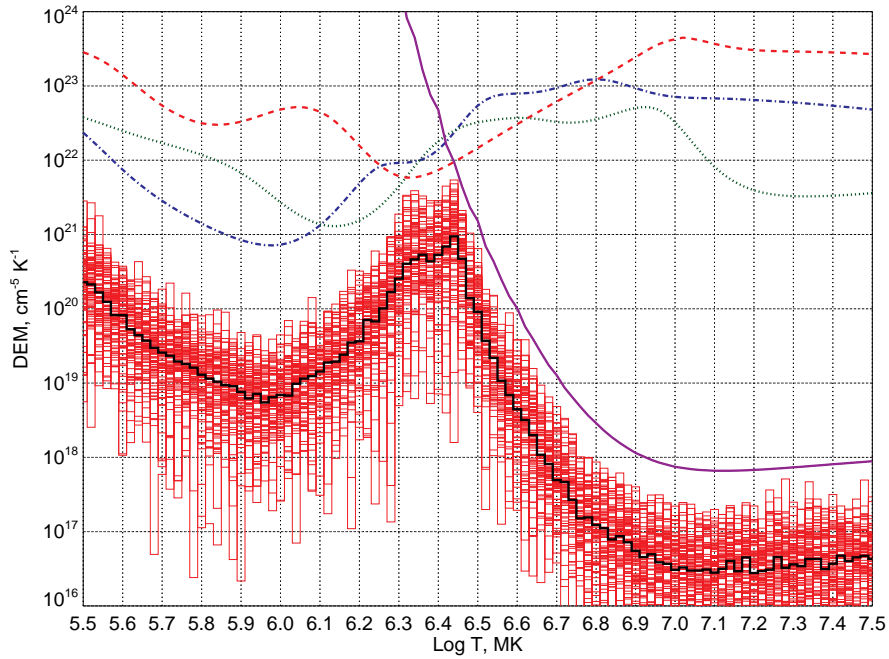


Figure 6. DEM of the non-flaring active region marked in Figure 5. Red: DEMs obtained during different runs of genetic algorithm; black: their median. Blue dashed dotted DEM-loci: EIT 171 Å; green dotted DEM-loci: EIT 195 Å; red dashed DEM-loci: EIT 284 Å; purple solid DEM-loci: Mg XII spectroheliograph.

The total uncertainties in the cross calibration should be a factor of three. Although this is a high value, it is lower than the errors of the DEM reconstruction (factor of ten). Therefore, in this work, we neglect the uncertainties of the cross-calibration.

4. Discussion

4.1. Nanoflare Frequency

In this section, we will compare our results with the results obtained in the numerical simulations of nanoflare heating.

Cargill (2014) performed numerical simulations of how a coronal loop should react to the sequence of nanoflares depending on the nanoflare frequency. The author found that for a low nanoflare frequency, the DEM has a hot component. The hot component vanishes for a high nanoflare frequency.

Cargill (2014) performed simulations for the following scenarios:

- nanoflares with power-law distribution of energies (slope $m = -2.5$) with a fixed delay between nanoflares;

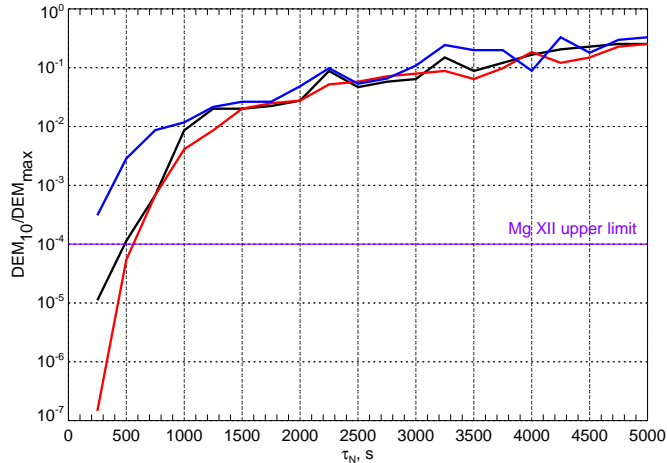


Figure 7. Ratio of the DEM_{10} to the DEM_{\max} as a function of the average time between nanoflares $[\tau_N]$. The data were taken from the simulation performed by Cargill (2014). Black line denotes the simulations where nanoflares have power-law energy distribution with a slope $m = -2.5$ and the delay between nanoflares is proportional to their energy. Red line denotes the simulations where nanoflares have power-law energy distribution with a slope $m = -1.5$ and the delay between nanoflares is proportional to their energy. Blue line denotes the simulations where nanoflares have power-law energy distribution with a slope $m = -2.5$ and the delay between nanoflares is fixed. Purple line denotes the Mg XII upper limit on the ratio of the DEMs of the hot and warm components.

- nanoflares with power-law distribution of energies (slope $m = -2.5$) with a delay between nanoflares that is proportional to the nanoflare energy;
- nanoflares with power-law distribution of energies (slope $m = -1.5$) with a delay between nanoflares that is proportional to the nanoflare energy.

For each of these regimes and different delays between nanoflares $[\tau_N]$, Cargill (2014) provided plots of the active region DEMs. For each of these plots, we manually measured the ratio of the DEM at 10 MK $[DEM_{10}]$ to the DEM of the main temperature component $[DEM_{\max}]$. Then we used the obtained values to build a plot of how this ratio depends on the delay between the nanoflares (see Figure 7).

As we see from Figure 7, the relative amount of hot plasma rapidly diminishes with the decrease of the delay between nanoflares. The Mg XII data shows that this ratio should be less than 10^{-4} . Therefore, the delay between the nanoflares should be less than 500 seconds.

We emphasize that the parameters of the active region picked for the DEM calculation in our work and the one picked for simulations in Cargill (2014) are different. Furthermore, the estimate of hot plasma based on the Mg XII data is only an upper limit that is accurate within an order of magnitude. Therefore, the value of the upper limit on the τ_N should be considered as a rough estimate.

There is another way to explain the absence of emission in the Mg XII images. If the heating impulse is very short, then the Mg ions could fail to reach the high-temperature ionization state before the electron temperature drops (Reale

and Orlando, 2008; Bradshaw, 2009). In this case, the hot emission will be absent not due to the low temperature, but due to the absence of the Mg XII ions.

4.2. Comparison with Other Observations

Table 1. Observations of the hot plasma in non-flaring active regions. DEM_X is a differential emission measure at temperature X MK.

Work	Instrument	Wavelength	$\frac{DEM_5}{DEM_3}$	$\frac{DEM_{10}}{DEM_3}$
Parenti <i>et al.</i> (2017)	SUMMER	Fe XIX 1118 Å	$\leq 0.1\%$	$\leq 0.1\%$
Del Zanna and Mason (2014)	FCS/SSM	13-20 Å	$\leq 1\%$	N/A
Hannah <i>et al.</i> (2016)	NuSTAR	2–78 keV	$\leq 10\%$	$\leq 0.1\%$
Ishikawa <i>et al.</i> (2014)	FOXSI	6–8 keV	$\leq 3\%$	$\leq 0.003\%$
Miceli <i>et al.</i> (2012)	SphinX	1.34–7 keV	N/A	N/A
Brosius, Daw, and Rabin (2014)	EUNIS-13	Fe XIX 592.2 Å	N/A	$\leq 7.6\%$
Sylwester, Sylwester, and Phillips (2010)	RESIK	3.4–6.1 Å	$\leq 0.1\%$	N/A
Winebarger <i>et al.</i> (2012)	XRT	2–40 Å	$\leq 10\%$	$\leq 10\%$
Warren, Winebarger, and Brooks (2012)	AIA	94 Å	$\leq 1–10\%$	$\leq 1–10\%$
This work	Mg XII/SPIRIT	Mg XII 8.42 Å	$\leq 0.01\%$	$\leq 0.001–0.01\%$

In this section, we will compare the results of our observations with the observations mentioned in the Introduction. For comparison, we listed in Table 1 the values of the DEM ratio of the hot and warm components of the active region. If the work did not have these values, we tried to recalculate them from the numbers listed in the articles.

Our observations and the observations listed in Table 1 exhibit a similar picture. Active regions are heated up to average temperatures around 3 MK. The steady hot plasma emission in non-flaring active regions is so faint that even the most sensitive instruments do not observe it. Heating above 3 MK is observed only during flares or microflares (Watanabe *et al.*, 1992; Sterling, Hudson, and Watanabe, 1997).

The Mg XII limit on the relative amount of the hot plasma is at least one order of magnitude lower than the limit obtained in previous works. Only the data obtained during the FOXSI mission have a comparable limit (Ishikawa *et al.*, 2014).

The advantages of the Mg XII data presented in this work are temperature selectivity and the continuous observations. The Mg XII data are monochromatic images of hot plasma that impose a strict constraints on the amount of hot plasma. Furthermore, the presented data are not just a few snapshots of the Sun; they represent thousands of images taken with a relatively high cadence.

The observations shows that hot plasma is systematically not observed in the non-flaring active regions.

Although the Mg XII data strictly constrained the amount of the hot plasma in non-flaring active regions, these observations are very old. Future instruments with better technology could improve the result.

4.3. Hot Plasma in Flaring Active Regions

Figure 3 shows that in flaring active regions the Mg XII emission does not go to zero between spikes. This emission corresponds to 4 DN per pixel, which is higher than the accuracy of the zero (0.5 DN), but lower than the noise (6 DN).

It is possible that this faint emission is caused by the nanoflares. However, it is also possible that this emission is the result of flares or microflares that previously occurred in the active region. Unfortunately, we do not have tools to distinguish these two cases.

5. Conclusion

In this work, we searched for hot plasma in the non-flaring active regions using the Mg XII spectroheliograph onboard CORONAS-F/SPIRIT. This instrument built monochromatic images of the solar corona in the Mg XII 8.42 Å line, which emits only at temperatures higher than 4 MK. The Mg XII images contain signal only from hot plasma without any low-temperature background.

Hot plasma was observed only in the flaring active regions or microflares. We did not observe any hot plasma in the non-flaring active regions. The hot plasma column emission measure in the non-flaring active region should not exceed $3 \times 10^{24} \text{ cm}^{-5}$.

The hot DEM of the non-flaring active region is less than 0.01 % of the DEM of the main temperature component. Absence of the Mg XII emission in the non-flaring active regions can be explained by weak and frequent nanoflares (delay less than 500 seconds) or by very short and intense nanoflares that lead to non-equilibrium of ionization.

This work proves neither presence nor absence of hot plasma in non-flaring active regions. It neither confirms nor discards the nanoflare-heating model. This work estimates an upper limit on the relative amount of hot and warm plasma in non-flaring active regions and compares it with the predictions of the numerical simulations. This comparison limits the possible nanoflare frequency, which could help in further development of the nanoflare-heating model.

Acknowledgments This research was supported by the Russian Science Foundation (project No. 17-12-01567).

Disclosure of Potential Conflicts of Interest

The authors declare that they have no conflicts of interest.

Appendix

A. Genetic Algorithm

DEM reconstruction is a problem of calculating DEM based on the experimental fluxes obtained in different spectral channels. The fluxes and DEM are connected with the formula

$$I_i = \int G_i(T) DEM(T) dT, \quad (3)$$

where I_i is an experimental flux in the channel i , $G_i(T)$ is the temperature response function of the channel i , $DEM(T)$ is the differential emission measure, and T is the temperature.

The genetic algorithm solves this problem by mimicking the process of the natural selection (Siarkowski *et al.*, 2008; Shestov, Reva, and Kuzin, 2014). It works in the following way:

- i) The algorithm creates 1000 random DEMs.
- ii) For each of the DEM, the algorithm calculates the fluxes using Equation 3.
- iii) Then the algorithm calculate a quantitative criteria of how well the calculated fluxes match with the experimental ones. As a quantitative criterion, we use χ^2 :

$$\chi^2 = \sum_i \frac{(C_i - I_i)^2}{\sigma_i^2}, \quad (4)$$

where C_i is a calculated flux in the channel i , I_i is an experimental flux in the channel i , and σ_i is measurement error of the flux in the channel i .

- iv) The algorithm selects 100 DEMs with the best χ^2 . The rest of the DEMs are deleted.
- v) The method creates 100 “mutated” DEMs: it copies the “best” DEMs and multiplies the value in each temperature bin by a random coefficient. This coefficient is uniformly distributed between 0.9 and 1.1.
- vi) The algorithm creates new 800 DEMs via “breeding”. This DEMs are calculated using the formula:

$$DEM = aDEM_1 + (1 - a)DEM_2, \quad (5)$$

where DEM is the new DEM obtained via “cross breeding”, DEM_1 and DEM_2 are two DEMs randomly picked from the set of the “best” DEMs, and a is a coefficient randomly picked from 0 to 1.

- vii) The algorithm repeats the procedure from the step ii) until the χ^2 of the best DEM stops changing.
- viii) When the χ^2 stops changing by more than 1%, the algorithm returns the best DEM as a result.

Equations 3 have an infinite number of solutions. A single run of the genetic algorithm randomly picks one solution. A second run will pick another solution, which will deviate from the first one. If we run the algorithm multiple times

and plot the obtained solutions, we can estimate the uncertainties of the DEM reconstruction (see Figure 6).

The proportion of the “best”, “mutated”, and “breeding” DEMs and the range of the coefficient that is used in the “mutating” procedure affect the speed of the calculation. We did not research which set of parameters is optimal. Most likely, there exists a better set of these parameters.

Sometimes the signal in some channels is below their sensitivity thresholds or a particular spectral line is blended with a stronger neighboring line. In this case, these channels provides only the upper limits on the fluxes. Equations 3 will change to:

$$I_i = \int G_i(T)DEM(T)dT \quad (6)$$

$$U_j \geq \int G_j(T)DEM(T)dT, \quad (7)$$

where I_i is the flux in the channel i , $G_i(T)$ is the temperature response function of the channel i , $DEM(T)$ is the differential emission measure, T is the temperature, U_j is the upper limit on the flux in the channel j , $G_j(T)$ is the temperature response function of the channel j .

Upper limits can enhance the DEM reconstruction. However, these limits cannot be treated like the usual fluxes. To use them, we need to modify the formula for calculating the χ^2 to

$$\chi^2 = \sum_i \frac{(C_i - I_i)^2}{\sigma_i^2} + \sum_j F(C_j, U_j) \quad (8)$$

where the function F is defined as

$$F(C_j, U_j) = \begin{cases} \frac{(C_j - U_j)^2}{U_j^2}, & C_j > U_j \\ 0, & C_j \leq U_j \end{cases} \quad (9)$$

F equals zero, when Equation 7 is satisfied, and F approaches zero as C_j approaches U_j .

References

- Biermann, L.: 1948, Über die Ursache der chromosphärischen Turbulenz und des UV-Exzesses der Sonnenstrahlung. *Zeit. Astrophys.* **25**, 161. ADS.
- Bradshaw, S.J.: 2009, A numerical tool for the calculation of non-equilibrium ionisation states in the solar corona and other astrophysical plasma environments. *Astron. Astrophys.* **502**, 409. DOI. ADS.
- Brosius, J.W., Daw, A.N., Rabin, D.M.: 2014, Pervasive Faint Fe XIX Emission from a Solar Active Region Observed with EUNIS-13: Evidence for Nanoflare Heating. *Astrophys. J.* **790**, 112. DOI. ADS.
- Cargill, P.J.: 1994, Some implications of the nanoflare concept. *Astrophys. J.* **422**, 381. DOI. ADS.
- Cargill, P.J.: 2014, Active Region Emission Measure Distributions and Implications for Nanoflare Heating. *Astrophys. J.* **784**, 49. DOI. ADS.

- Davila, J.M.: 1987, Heating of the solar corona by the resonant absorption of Alfvén waves. *Astrophys. J.* **317**, 514. DOI. ADS.
- Del Zanna, G., Mason, H.E.: 2014, Elemental abundances and temperatures of quiescent solar active region cores from X-ray observations. *Astron. Astrophys.* **565**, A14. DOI. ADS.
- Del Zanna, G., O'Dwyer, B., Mason, H.E.: 2011, SDO AIA and Hinode EIS observations of “warm” loops. *Astron. Astrophys.* **535**, A46. DOI. ADS.
- Delaboudinière, J., Artzner, G.E., Brunaud, J., Gabriel, A.H., Hochedez, J.F., Millier, F., Song, X.Y., Au, B., Dere, K.P., Howard, R.A., Kreplin, R., Michels, D.J., Moses, J.D., Defise, J.M., Jamar, C., Rochus, P., Chauvineau, J.P., Marioge, J.P., Catura, R.C., Lemen, J.R., Shing, L., Stern, R.A., Gurman, J.B., Neupert, W.M., Maucherat, A., Clette, F., Cugnon, P., van Dessel, E.L.: 1995, EIT: Extreme-Ultraviolet Imaging Telescope for the SOHO Mission. *Solar Phys.* **162**, 291. DOI. ADS.
- Dere, K.P., Landi, E., Mason, H.E., Monsignori Fossi, B.C., Young, P.R.: 1997, CHIANTI - an atomic database for emission lines. *Astron. Astrophys. Suppl.* **125**, 149. DOI. ADS.
- Dere, K.P., Moses, J.D., Delaboudinière, J.-P., Brunaud, J., Carabetian, C., Hochedez, J.-F., Song, X.Y., Catura, R.C., Clette, F., Defise, J.-M.: 2000, The Preflight Photometric Calibration of the Extreme-Ultraviolet Imaging Telescope EIT. *Solar Phys.* **195**, 13. DOI. ADS.
- Domingo, V., Fleck, B., Poland, A.I.: 1995, The SOHO Mission: an Overview. *Solar Phys.* **162**, 1. DOI. ADS.
- Gburek, S., Sylwester, J., Kowalinski, M., Bakala, J., Kordylewski, Z., Podgorski, P., Plocieniak, S., Siarkowski, M., Sylwester, B., Trzebinski, W., Kuzin, S.V., Pertsov, A.A., Kotov, Y.D., Farnik, F., Reale, F., Phillips, K.J.H.: 2011, SphinX soft X-ray spectrophotometer: Science objectives, design and performance. *Solar Sys. Res.* **45**, 189. DOI. ADS.
- Golub, L., Deluca, E., Austin, G., Bookbinder, J., Caldwell, D., Cheimets, P., Cirtain, J., Cosmo, M., Reid, P., Sette, A., Weber, M., Sakao, T., Kano, R., Shibasaki, K., Hara, H., Tsuneta, S., Kumagai, K., Tamura, T., Shimojo, M., McCracken, J., Carpenter, J., Haight, H., Siler, R., Wright, E., Tucker, J., Rutledge, H., Barbera, M., Peres, G., Varisco, S.: 2007, The X-Ray Telescope (XRT) for the Hinode Mission. *Solar Phys.* **243**, 63. DOI. ADS.
- Hannah, I.G., Grefenstette, B.W., Smith, D.M., Glesener, L., Krucker, S., Hudson, H.S., Madsen, K.K., Marsh, A., White, S.M., Caspi, A., Shih, A.Y., Harrison, F.A., Stern, D., Boggs, S.E., Christensen, F.E., Craig, W.W., Hailey, C.J., Zhang, W.W.: 2016, The First X-Ray Imaging Spectroscopy of Quiescent Solar Active Regions with NuSTAR. *Astrophys. J. Lett.* **820**, L14. DOI. ADS.
- Harrison, F.A., Craig, W.W., Christensen, F.E., Hailey, C.J., Zhang, W.W., Boggs, S.E., Stern, D., Cook, W.R., Forster, K., Giommi, P., Grefenstette, B.W., Kim, Y., Kitaguchi, T., Koglin, J.E., Madsen, K.K., Mao, P.H., Miyasaka, H., Mori, K., Perri, M., Pivovarov, M.J., Puccetti, S., Rana, V.R., Westergaard, N.J., Willis, J., Zoglauer, A., An, H., Bachetti, M., Barrière, N.M., Bellm, E.C., Bhalerao, V., Brejnholt, N.F., Fuerst, F., Liebe, C.C., Markwardt, C.B., Nynka, M., Vogel, J.K., Walton, D.J., Wik, D.R., Alexander, D.M., Cominsky, L.R., Hornschemeier, A.E., Hornstrup, A., Kaspi, V.M., Madejski, G.M., Matt, G., Molendi, S., Smith, D.M., Tomsick, J.A., Ajello, M., Ballantyne, D.R., Baloković, M., Barret, D., Bauer, F.E., Blandford, R.D., Brandt, W.N., Brenneman, L.W., Chiang, J., Chakrabarty, D., Chenevez, J., Comastri, A., Dufour, F., Elvis, M., Fabian, A.C., Farrah, D., Fryer, C.L., Gotthelf, E.V., Grindlay, J.E., Helfand, D.J., Krivonos, R., Meier, D.L., Miller, J.M., Natalucci, L., Ogle, P., Ofek, E.O., Ptak, A., Reynolds, S.P., Rigby, J.R., Tagliaferri, G., Thorsett, S.E., Treister, E., Urry, C.M.: 2013, The Nuclear Spectroscopic Telescope Array (NuSTAR) High-energy X-Ray Mission. *Astrophys. J.* **770**, 103. DOI. ADS.
- Ishikawa, S., Glesener, L., Christe, S., Ishibashi, K., Brooks, D.H., Williams, D.R., Shimojo, M., Sako, N., Krucker, S.: 2014, Constraining hot plasma in a non-flaring solar active region with FOXSI hard X-ray observations. *Pub. Astron. Soc. Japan* **66**, S15. DOI. ADS.
- Klimchuk, J.A.: 2006, On Solving the Coronal Heating Problem. *Solar Phys.* **234**, 41. DOI. ADS.
- Klimchuk, J.A.: 2015, Key aspects of coronal heating. *Phil. Trans. Roy. Soc. London Ser. A* **373**, 20140256. DOI. ADS.
- Krucker, S., Christe, S., Glesener, L., Ishikawa, S., Ramsey, B., Takahashi, T., Watanabe, S., Saito, S., Gubarev, M., Kilaru, K., Tajima, H., Tanaka, T., Turin, P., McBride, S., Glaser, D., Fermin, J., White, S., Lin, R.: 2014, First Images from the Focusing Optics X-Ray Solar Imager. *Astrophys. J. Lett.* **793**, L32. DOI. ADS.

- Lemen, J.R., Title, A.M., Akin, D.J., Boerner, P.F., Chou, C., Drake, J.F., Duncan, D.W., Edwards, C.G., Friedlaender, F.M., Heyman, G.F., Hurlburt, N.E., Katz, N.L., Kushner, G.D., Levay, M., Lindgren, R.W., Mathur, D.P., McFeaters, E.L., Mitchell, S., Rehse, R.A., Schrijver, C.J., Springer, L.A., Stern, R.A., Tarbell, T.D., Wuelser, J.-P., Wolfson, C.J., Yanari, C., Bookbinder, J.A., Cheimets, P.N., Caldwell, D., DeLuca, E.E., Gates, R., Golub, L., Park, S., Podgorski, W.A., Bush, R.I., Scherrer, P.H., Gumm, M.A., Smith, P., Aufer, G., Jerram, P., Pool, P., Souffi, R., Windt, D.L., Beardsley, S., Clapp, M., Lang, J., Waltham, N.: 2012, The Atmospheric Imaging Assembly (AIA) on the Solar Dynamics Observatory (SDO). *Solar Phys.* **275**, 17. DOI. ADS.
- Miceli, M., Reale, F., Gburek, S., Terzo, S., Barbera, M., Collura, A., Sylwester, J., Kowalinski, M., Podgorski, P., Gryciuk, M.: 2012, X-ray emitting hot plasma in solar active regions observed by the SphinX spectrometer. *Astron. Astrophys.* **544**, A139. DOI. ADS.
- Oraevsky, V.N., Sobelman, I.I.: 2002, Comprehensive Studies of Solar Activity on the CORONAS-F Satellite. *Astron. Lett.* **28**, 401. DOI. ADS.
- Parenti, S., del Zanna, G., Petralia, A., Reale, F., Teriaca, L., Testa, P., Mason, H.E.: 2017, Spectroscopy of Very Hot Plasma in Non-flaring Parts of a Solar Limb Active Region: Spatial and Temporal Properties. *Astrophys. J.* **846**, 25. DOI. ADS.
- Parker, E.N.: 1988, Nanoflares and the solar X-ray corona. *Astrophys. J.* **330**, 474. DOI. ADS.
- Reale, F., Orlando, S.: 2008, Nonequilibrium of Ionization and the Detection of Hot Plasma in Nanoflare-heated Coronal Loops. *Astrophys. J.* **684**, 715. DOI. ADS.
- Reale, F., Testa, P., Klimchuk, J.A., Parenti, S.: 2009, Evidence of Widespread Hot Plasma in a Nonflaring Coronal Active Region from Hinode/X-Ray Telescope. *Astrophys. J.* **698**, 756. DOI. ADS.
- Reale, F., Guarrasi, M., Testa, P., DeLuca, E.E., Peres, G., Golub, L.: 2011, Solar Dynamics Observatory Discovers Thin High Temperature Strands in Coronal Active Regions. *Astrophys. J. Lett.* **736**, L16. DOI. ADS.
- Reva, A., Shestov, S., Bogachev, S., Kuzin, S.: 2012, Investigation of Hot X-Ray Points (HXPs) Using Spectroheliograph Mg xii Experiment Data from CORONAS-F/SPIRIT. *Solar Phys.* **276**, 97. DOI. ADS.
- Reva, A., Shestov, S., Zimovets, I., Bogachev, S., Kuzin, S.: 2015, Wave-like Formation of Hot Loop Arcades. *Solar Phys.* **290**, 2909. DOI. ADS.
- Schmelz, J.T., Saar, S.H., DeLuca, E.E., Golub, L., Kashyap, V.L., Weber, M.A., Klimchuk, J.A.: 2009a, Hinode X-Ray Telescope Detection of Hot Emission from Quiescent Active Regions: A Nanoflare Signature? *Astrophys. J. Lett.* **693**, L131. DOI. ADS.
- Schmelz, J.T., Kashyap, V.L., Saar, S.H., Dennis, B.R., Grigis, P.C., Lin, L., De Luca, E.E., Holman, G.D., Golub, L., Weber, M.A.: 2009b, Some Like It Hot: Coronal Heating Observations from Hinode X-ray Telescope and RHESSI. *Astrophys. J.* **704**, 863. DOI. ADS.
- Schwarzschild, M.: 1948, On Noise Arising from the Solar Granulation. *Astrophys. J.* **107**, 1. DOI. ADS.
- Shestov, S., Reva, A., Kuzin, S.: 2014, Extreme Ultraviolet Spectra of Solar Flares from the Extreme Ultraviolet Spectroheliograph SPIRIT Onboard the CORONAS-F Satellite. *Astrophys. J.* **780**, 15. DOI. ADS.
- Siarkowski, M., Falewicz, R., Kepa, A., Rudawy, P.: 2008, Diagnostic of the temperature and differential emission measure (DEM) based on Hinode/XRT data. *Ann. Geophys.* **26**, 2999. DOI. ADS.
- Sterling, A.C., Hudson, H.S., Watanabe, T.: 1997, Electron Temperatures of the Corona Above a Solar Active Region Determined from S XV Spectra. *Astrophys. J. Lett.* **479**, L149. DOI. ADS.
- Sylwester, B., Sylwester, J., Phillips, K.J.H.: 2010, Soft X-ray coronal spectra at low activity levels observed by RESIK. *Astron. Astrophys.* **514**, A82. DOI. ADS.
- Sylwester, J., Gaicki, I., Kordylewski, Z., Kowaliński, M., Nowak, S., Plocieniak, S., Siarkowski, M., Sylwester, B., Trzebiński, W., Bakala, J., Culhane, J.L., Whyndham, M., Bentley, R.D., Guttridge, P.R., Phillips, K.J.H., Lang, J., Brown, C.M., Doschek, G.A., Kuznetsov, V.D., Oraevsky, V.N., Stepanov, A.I., Lisin, D.V.: 2005, Resik: A Bent Crystal X-ray Spectrometer for Studies of Solar Coronal Plasma Composition. *Solar Phys.* **226**, 45. DOI. ADS.
- Testa, P., Reale, F.: 2012, Hinode/EIS Spectroscopic Validation of Very Hot Plasma Imaged with the Solar Dynamics Observatory in Non-flaring Active Region Cores. *Astrophys. J. Lett.* **750**, L10. DOI. ADS.

- Testa, P., Reale, F., Landi, E., DeLuca, E.E., Kashyap, V.: 2011, Temperature Distribution of a Non-flaring Active Region from Simultaneous Hinode XRT and EIS Observations. *Astrophys. J.* **728**, 30. DOI. ADS.
- Urnov, A.M., Shestov, S.V., Bogachev, S.A., Goryaev, F.F., Zhitnik, I.A., Kuzin, S.V.: 2007, On the spatial and temporal characteristics and formation mechanisms of soft X-ray emission in the solar corona. *Astron. Lett.* **33**, 396. DOI. ADS.
- Viereck, R.A., Machol, J.L.: 2017, Solar X-Ray Irradiance Observations from the NOAA GOES Spacecraft: Accuracy vs Continuity. *AGU Fall Meeting Abstracts*. ADS.
- Warren, H.P., Winebarger, A.R., Brooks, D.H.: 2012, A Systematic Survey of High-temperature Emission in Solar Active Regions. *Astrophys. J.* **759**, 141. DOI. ADS.
- Watanabe, T., Hiei, E., Lang, J., Culhane, J.L., Bentley, R.D., Doschek, G.A., Bromage, B.J.I., Brown, C.M., Feldman, U., Fludra, A., Kato, T., Payne, J.: 1992, Helium-like sulphur emission lines in solar active regions and their sub-C class variability. *Pub. Astron. Soc. Japan* **44**, L141. ADS.
- White, S.M., Thomas, R.J., Schwartz, R.A.: 2005, Updated Expressions for Determining Temperatures and Emission Measures from Goes Soft X-Ray Measurements. *Solar Phys.* **227**, 231. DOI. ADS.
- Wilhelm, K., Curdt, W., Marsch, E., Schühle, U., Lemaire, P., Gabriel, A., Vial, J.-C., Grewing, M., Huber, M.C.E., Jordan, S.D., Poland, A.I., Thomas, R.J., Kühne, M., Timothy, J.G., Hassler, D.M., Siegmund, O.H.W.: 1995, SUMER - Solar Ultraviolet Measurements of Emitted Radiation. *Solar Phys.* **162**, 189. DOI. ADS.
- Winebarger, A.R., Warren, H.P., Schmelz, J.T., Cirtain, J., Mulu-Moore, F., Golub, L., Kobayashi, K.: 2012, Defining the “Blind Spot” of Hinode EIS and XRT Temperature Measurements. *Astrophys. J. Lett.* **746**, L17. DOI. ADS.
- Zhitnik, I.A., Bougaenko, O.I., Delaboudiniere, J.-P., Ignatiev, A.P., Korneev, V.V., Krutov, V.V., Kuzin, S.V., Lisin, D.V., Mitrofanov, A.V., Oparin, S.N., Oraevsky, V.N., Pertsov, A.A., Slemzin, V.A., Sobelman, I.I., Stepanov, A.I., Schwarz, J.: 2002, SPIRIT X-ray telescope/spectroheliometer results. In: A. Wilson (ed.) *Solar Variability: From Core to Outer Frontiers*, ESA, Noordwijk **SP-506**, 915. ADS.
- Zhitnik, I.A., Bougaenko, O.I., Ignat'ev, A.P., Krutov, V.V., Kuzin, S.V., Mitrofanov, A.V., Oparin, S.N., Pertsov, A.A., Slemzin, V.A., Stepanov, A.I., Urnov, A.M.: 2003, Dynamic 10 MK plasma structures observed in monochromatic full-Sun images by the SPIRIT spectroheliograph on the CORONAS-F mission. *Mon. Not. Roy. Astron. Soc.* **338**, 67. DOI. ADS.